Applied Surface Science 349 (2015) 403–414

Contents lists available at ScienceDirect

Applied Surface Science

journal homepage: www.elsevier.com/locate/apsusc

Plasma nitriding of HP13Cr supermartensitic stainless steel

Bruna C.E.S. Kurelo[a], Gelson B. de Souza[a,*], Silvio L. Rutz da Silva[a], Francisco C. Serbena[a], Carlos E. Foerster[a], Clodomiro Alves Jr.[b]

[a] Department of Physics, Universidade Estadual de Ponta Grossa, Av. Gen. Carlos Cavalcanti n° 4748, 84.030-000 Ponta Grossa, PR, Brazil
[b] Department of Mechanical Engineering, Universidade Federal do Rio Grande do Norte, Campus Universitário s/n, 59072-970 Natal, RN, Brazil

ARTICLE INFO

Article history:
Received 9 January 2015
Received in revised form 10 April 2015
Accepted 30 April 2015
Available online 6 May 2015

Keywords:
Plasma nitriding
Supermartensitic stainless steel
Surface
Hardness
Elastic modulus
Scratch test

ABSTRACT

Supermartensitic stainless steels (SMSS) are commonly employed in the oil exploitation industry and present a good balance between the necessary physical and chemical properties and financial costs. Certain applications, such as in extreme corrosive and abrasive environments, demand improvements in the surface properties of these steels. In the present work, HP13Cr SMSS with a fully martensitic microstructure were plasma nitrided in the 350–450 °C range. The high diffusivity and low solubility of nitrogen in the martensitic structure allowed the production of thick layers (16–61 μm) containing ε-$Fe_{2-3}N$, γ′-Fe_4N and expanded phase (α_N) in all the temperatures. In addition, anisotropic sputtering rate and N-diffusion were observed for different grain orientations. Mechanical properties were measured by instrumented indentation, appropriately corrected from roughness effects on the results. Hardness profiles increased from 3.8 GPa (bulk) to ~14 GPa (near surface region) in all the working temperatures, whereas the elastic modulus was 230 GPa, presenting no statistically significant differences with respect to the bulk value. Nanoscratch tests revealed a hardened-ductile like behavior of these nitride layers. The surface tribo-mechanical behavior was correlated with elastic–plastic responses of the precipitate-containing texturized layers. Results are interpreted in light of the effectiveness of plasma nitriding to modify the surface properties of SMSS.

1. Introduction

Supermartensitic stainless steels (SMSS) are currently used by the petrochemistry industry in gas and oil pipelines for the deep sea environment, subjected to high temperatures and pressures in the presence of corrosive agents such CO_2, H_2S and Cl^- [1–4].

SMSS belong to the Fe–Cr–Ni–Mo system with relatively low percentage of alloying elements. As an economic alternative to austenitic and duplex steels, SMSS oil pipes present reduced wall thickness and weight, with improved mechanical properties, weldability and corrosion resistance. These features are obtained on SMSS by controlling the alloying elements and the austenite/martensite volume ratio. Particularly, the enhanced SMSS weldability is due to the low carbon content of 0.02 wt% or less. Besides, the lower carbon content and the addition of Mo (~2 wt%), together with the 13% Cr, helps to promote corrosion protection in the aggressive crude oil and seawater environment [1,3,5–7]. The low C concentration requires increased Ni content up to around 6%, which stabilizes austenite in higher temperatures [1,3]. The Cr/Ni ratio promotes the formation of martensitic microstructure with retained austenite, which can be controlled by appropriate heat and tempering treatments. Zou and co-workers [4], investigating the tempering process effects on 13Cr–4Ni–1Mo SMSS, reported that the microstructure with 11.5% retained austenite promoted the best results for tensile and yield strength, elongation and hardness.

Much effort has been made to improve the SMSS bulk properties. The material's thermal history is a determinant parameter for its mechanical performance, since unwanted α- and δ-ferrite precipitates can cause strength reduction. Such concern is critical in welding, that locally alters the microstructure in the heat affected zones [8,9], besides favoring hydrogen induced cracking [2,7,10]. Precipitation of intermetallic compounds such as Fe_2Mo can also deteriorate the SMSS mechanical strength. Otherwise, a modified composition with 0.13% Ti was reported to present, after tempering, fine Ti(C,N) particles dispersed in a martensitic matrix, with superior mechanical properties than the Ti-free SMSS [6].

The surface properties of SMSS used in gas and oil pipelines also demand attention when employed in aggressive environments. In recent years, oil deposits have been discovered and aimed to exploitation in rock layers lying thousands of meters beneath deep seas. The Pre-salt layer, an oil field in the Brazil offshore coast, is

* Corresponding author. Tel.: +55 42 3220 3044; fax: +55 42 3220 3042.
E-mail addresses: gelsonbs@uepg.br, gelbsou@yahoo.com.br, gelsonbs@gmail.com (G.B. de Souza).

http://dx.doi.org/10.1016/j.apsusc.2015.04.202
0169-4332/

believed to accumulate 10^9 barrels of oil and gas, situated around 7000 m depth (the ocean floor is 2000–3000 m from the surface) [11]. High pressures and temperatures and abundant corrosive elements must be challenged to reach reservoirs situated in the midst of a thick and deep salt layer. Besides, intense abrasion occurs in the pipe's interior walls by sand particles mixed with oil. In the Pre-salt layer, special steels are also demanded as raw materials for valves, connection points and peripheral devices of "subsea trees", which control the oil pump from the wellbore to the platform above.

The formation of nitride precipitates and/or expanded phases by plasma-based ion implantation processes can altogether afford significant improvements on the surface mechanical and tribological features of stainless steels [12–15]. Hardness can be raised as high as five times, whereas friction and wear rate decreases around one order of magnitude [16,17]. These results were observed for a wide variety of steels such as ferritic, austenitic, and duplex ones.

In the case of martensitic stainless steels, previous works corroborate the surface protective effects of plasma-based treatments as well. A known effect of PN is the production of a nitrogen expanded phase (termed S-phase) in austenitic steels [18]; similarly, Kim et al. [19] found that expanded martensite, in analogy to the expanded austenite, was produced on AISI 420 steel submitted to RF plasma nitriding at 400 °C, resulting in a surface hardness increase of 4.3 times. A carbon expanded martensite, in addition to Fe_3C precipitates, was reported for AISI 420 submitted to plasma carburizing [20]. This same martensitic steel, submitted to PN at temperatures in the range 480–560 °C, presented a compound layer structure containing fine and homogeneous precipitates of Fe_4N, $Fe_{2-3}N$, CrN over a diffusion zone [21]. Results obtained with other plasma-based treatments [22–24] are also suggestive of improving the tribological performance of martensitic stainless steels. Specifically on SMSS, Fernandes et al. [25] observed that wear rates decreased with heat treatments in the range 400–500 °C in samples submitted to PN, and in samples treated by plasma nitriding and carburizing (PNC).

The nitriding effects to the anti-corrosion properties of stainless steels are taken into consideration as well [26,27]. The heating parameters involved in nitriding can compromise the corrosion resistance of these alloys, as observed by [28,29]. Thus, the control of the plasma treatment conditions can lead to phases that promote corrosion resistance, as well as to prevent sensitization (chromium depletion) [18].

The present work focuses on the DC plasma nitriding of the SMSS HP13-Cr. The mechanical properties and scratch resistance were characterized at nanoscale and correlated with morphological and microstructure modifications running at the near surface region. Because several martensite to austenite ratios can be achieved in the bulk SMSS and hence influence in different manners the surface mechanical response, here, the nitriding processes were performed in samples with fully martensitic microstructure.

2. Experimental procedure

2.1. Sample preparation

Samples with 15 mm × 15 mm × 2 mm (height × width × thickness) were cut from a block of supermartensitic stainless steel HP13Cr, with composition (wt%) 13%Cr, 5% Ni, 0.45% Mn, 2% Mo, 0.025% C.

Since several martensite/austenite mixtures are allowed in SMSS, and because the substrate beneath modified surfaces strongly affects their mechanical and tribological responses [30], the samples microstructures were initially homogenized prior to nitriding. This procedure intends to rule out spurious effects from the many possible bulk conditions, focusing on the surface tribo-mechanical response for a pristine SMSS. The fully martensitic microstructure was achieved by a two-step heat treatment [1,31,32]. The first one was the *austenitizing* into a preheated furnace, with subsequent *quenching*. The optimal conditions for these processes were investigated by heating samples up to 975, 1000, 1025 and 1100 °C for 30 min, in air, with subsequent quenching in a bath of distilled water and ice at 0 °C. An additional batch was prepared where samples were heated at the same previous temperatures and then quenched in mineral oil at 20 °C. Both water and oil were contained in 1 L beakers. These methods changed the steel microstructure to austenite (above 950 °C) with subsequent rapid transformation to martensite [9,33]. The second step was the *tempering*, carried out concomitantly with the nitriding process in the plasma chamber, which temperatures correspond to the tempering range for steels [31,32]. It is worth mention that such process does not affect the diffusion kinetics during nitriding, since metastable atoms in the lattice shifts to the equilibrium [34]. In this report, samples nominated as "Reference" correspond to the not nitrided ones, picked from the austenitized and quenched samples treated in the best conditions found in step 1, as discussed in Section 3.1, and tempered inside a furnace under Argon atmosphere at 400 °C for 6 h.

After austenitizing and tempering, samples were polished to mirror finishing by grinding using successive SiC papers up to P1200, and final polishing up to 1 μm diamond paste, followed by a final polishing in colloidal silica solution with 85 vol.% of H_2O_2. Cleaning was performed twice in ultrasound bath using acetone for 15 min.

2.2. Plasma nitriding

The SMSS samples were nitrided in a custom-made DC glow discharge (GD) system, consisting of a chamber, vacuum system, power supply, and pressure and temperature controllers. Aiming to remove contaminants and oxides from the surface, pre-sputtering treatment was performed in H_2 atmosphere at 150 ± 10 °C for 1 h, at 300 Pa pressure. The nitriding atmosphere was a mixture of 20% N_2 80% H_2 (vol.), with gas inlet 4 sccm and 16 sccm, respectively and total pressure kept 300 Pa. The working temperatures were measured using a backside thermocouple and controlled using the plasma current (in the range 200–300 mA). At these conditions, the voltage ranged from 370 to 407 V according to the nitriding temperature. The average ion energy in glow discharge systems can be estimated by means of the L/λ ratio, where L is the sheath width and λ the mean free path [35]. In the present situation, L is about 1.5 mm, λ can be estimated as ~0.5 mm, and therefore $L/\lambda \sim 3$. As a result, the average ion energy for the employed voltages is about 250 eV. Three samples batches were prepared, using the same treatment time (6 h) and different temperatures:

(i) 350 °C
(ii) 400 °C
(iii) 450 °C

Temperature fluctuations were at most ±10 °C in all the situations.

2.3. Crystalline structure and morphology

Structural changes were characterized by X-ray diffraction – XRD (Rigaku Ultima IV) with CuK_α radiation (λ = 0.15406 nm) under the Bragg–Brentano (θ–2θ) geometry. The diffractograms were obtained in the range 30–90° with 0.02° steps and a counting time of 4 s at each step. The diffraction peaks were identified according to powder crystallographic data, with the following PDF card numbers: 33-397 (γ-austenite); 34-396 (α'-martensite); 86-231

(γ'-Fe_4N); 49-1664 and 72-2126 (ε-$Fe_{2-3}N$); 76-2494 (CrN); 35-783 ($Cr_{23}C_6$); 80-1701 ($Mn_{23}C_6$); 36-1482 (Cr_7C_3); 75-1499 (Fe_7C_3); 80-1699 (Mn_7C_3); 76-1877 (Fe_3C). The α_N (expanded martensite) was identified according to Kim et al. [19].

Topography and roughness were analyzed by atomic force microscopy – AFM (Shimadzu SPM 9600) operating in contact mode.

The indentation imprints and scratch grooves were imaged by a field emission scanning electron microscopy – FEG-SEM (Tescan Mira 3) and SEM (Jeol JSM-6360 LV). Elemental analyses were obtained by energy-dispersive spectroscopy – EDS (Oxford XMaxN SDD) operating at 20 kV. The electron beam spot size in EDS analyses was 69 nm. To visualize the produced layers, cross-sectioned samples were etched with Vilela's and Murakami's reagents and analyzed by FEG-SEM and optical microscopy (Olympus bx51), respectively.

2.4. Mechanical properties

Hardness and elastic modulus profiles were obtained by using a NanoIndenter XP (MTS), following the well-established Oliver–Pharr method [36]. A pyramidal Berkovich-type diamond tip was employed, calibrated with fused-silica sample with known properties (H = 9.5 GPa and E = 73.0 GPa). Loads varied from 0.8 to 400 mN in 10 successive loading-unloading cycles. Each sample was indented at 40 different sites, 100 μm apart one from another.

The intense sputtering taking place in plasma-based processes results in peaks and valleys on the surfaces with varied height distribution. The indenter tip and asperity interactions cause errors in the Oliver–Pharr analytical method, which was developed for flat surfaces. In order to minimize such problem, a contact stiffness analysis was applied on the indentation data, which corrects the zero tip contact depth in the loading-unloading curves [37]. The conventional method [36] was subsequently reapplied to calculate hardness and elastic modulus of the nitrided surfaces.

In order to investigate hardening effects in deeper regions on the modified surfaces, additional microhardness tests (Hoatec Inc.) were carried out using a Vickers indenter and loads in the range 1000–20,000 mN. Hardness in the Oliver and Pharr method is obtained from the ratio between load (P_{max}) and the *projected area* ($A_{projected}$) of a Berkovich tip (the triangular base) *during contact* [36], whereas Vickers hardness is determined *after the load relief* and using the contact area of the square based pyramid faces with the material [34]. Aiming to minimize differences in the calculated profiles, here an approaching to the Oliver and Pharr definition was considered for microhardness tests, $H_{vickers}$:

$$H_{vickers} = \frac{P_{max}}{A_{projected}} = \frac{P_{max}}{d^2/2} \quad (1)$$

where d is the averaged diagonal of the imprint-projected area, as visualized by a microscope.

As additional investigations, single loading instrumented indentations were carried out directly on the sample's cross sections with 200 mN applied load.

2.5. Nanoscratch tests

Scratch tests were performed with the same instrumented indentation facility, following the Berkovich-tip edge direction with scratch velocity of 10 μm/s and 600 μm length. The initial surface morphology was obtained by scanning the track under a 50 μN constant load; then, the tip displacement profile was monitored during scratching up to 400 mN with constant loading rate (6.7 mN/s). After that, the groove morphology was once again verified (the residual depth) under 50 μN load. The *penetration profiles* correspond to the displacement curves subtracted from the original profile. For each loading condition, the surfaces were tested at three different locations.

3. Results and discussion

3.1. Crystalline structure

Before plasma nitriding, the SMSS samples were submitted to austenitizing and quenching treatments.

Fig. 1 shows XRD diffractograms of the pristine and the heated SMSS samples at different temperatures and quenched in (a) water and (b) oil. The as-received material presented diffraction peaks ascribed to martensite (α') and austenite (γ) phases. In Fig. 1a (oil quenching), after heating at 975 °C and 1025 °C, the γ phase vanished, whereas peaks with small intensities indicated that carbides were precipitated in the matrix. According to the phase diagram of this alloy [33], the carbide phases comprise the $M_{23}C_6$, M_7C_3, and M_3C stoichiometries, where M corresponds to a metal atom from the alloy. If chromium is segregated to form these compounds, they will form Cr_2O_3 at the surface, depleting the bulk and affecting the corrosion resistance of the material [38]. Such carbides are formed due to the carbon availability in the material [9], despite

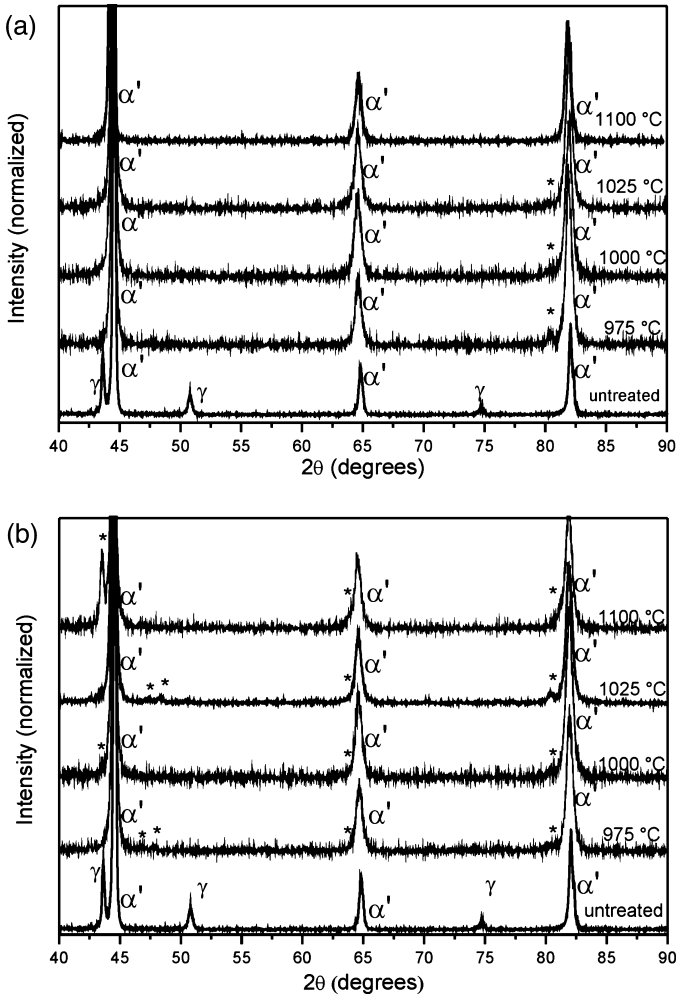

Fig. 1. X-ray diffractograms of SMSS samples submitted to austenitizing and heat-treatments, carried out previously to the plasma nitriding process. The as-received (untreated) material presented contributions of martensite and austenite. The fully martensitic microstructure was attained at the indicated temperatures, with subsequent quenching in (a) mineral oil and (b) distilled water. The carbide phases (*) comprise $M_{23}C_6$, M_7C_3, and M_3C stoichiometries, where M correspond to a metal atom. α' = martensite; γ = austenite.

the small C-amount in the alloy (~0.01 wt%). It is worth mentioning that samples were grounded *after* austenitizing and quenching in order to remove the reaction layer produced by the heating/cooling processes. Moreover, carbon mobility is faster in martensite as compared to austenite, as latter resumed in Section 3.2. Otherwise, carbides were not identified in the sample austenitized at 1100 °C. There are important factors affecting the alloy at this temperature that can prevent carbide precipitation in large amounts. At 1100 °C, the crystalline structure was fully austenitic [33] and the chromium diffusivity was enhanced [39]. Moreover, according to Durham et al. [38], the carbide dissolution takes place at such thermodynamic conditions.

The treatments with subsequent quenching in water (Fig. 1b) presented the same features as observed for the oil quenching. However, carbides were precipitated regardless the austenitizing temperature because of the reduced cooling efficiency, since water has a lower heat capacity than the mineral oil.

The above results indicated that the heat treatment at 1100 °C followed by oil quenching was effective in obtaining a fully martensitic microstructure, with less significant (not detectable) carbide precipitation. Thus, initially the SMSS samples were submitted to this protocol, whereas the tempering was achieved concomitantly with the plasma nitriding process. For comparison purposes, the SMSS reference sample (untreated) was austenitized and quenched, and subsequently tempered in Argon atmosphere in conditions similar to the nitriding ones. In the analysis presented subsequently, several effects will be correlated with the pristine martensitic microstructure of the material. It is important to mention that in $\alpha' + \gamma$ containing SMSS, tailored for application purposes, martensite is the predominant microstructure with a concentration above 85% [4].

Fig. 2 shows X-ray diffractograms of the reference sample and the SMSS plasma nitrided at the indicated temperatures. The diffractograms of nitrided SMSS disclosed more substantial changes than the observed in similar treatments of austenitic steels [16,40]. The broad peaks at ~43° and ~64° in the lower temperatures, 350 °C and 400 °C, can be atributted to the nitrogen-expanded martensite phase (α_N), which comprises several Fe(N) sub-estoichiometries. Fe(N) is a metastable, precipitate-free and supersaturated phase produced by the interstitial Nitrogen into the α' matrix [18]. Differently from austenitic steels, γ'-Fe_4N and ε-$Fe_{2+x}N$ phases were formed in SMSS even at the lowest temperature, 350 °C. The presence of nitride phases in the diffractograms increased with temperature as the α_N decreased. The ε-$Fe_{2+x}N$ ($0 \leq x \leq 1$) compound comprises several stoichiometries from Fe_2N to Fe_3N, also resulting in broad peaks.

The above results are justified based on the intrinsic differences between the body-centered tetragonal martensite (α') and the fcc-austenite (γ) structures. Concerning the nitrogen solubility, the γ microstructure (fcc) differs from the ferrite (bcc) because it presents larger octahedral interstices to accommodate the N-atoms [41]. For instance, the reported concentrations at 590 °C are 2.4 and 0.1 wt%, respectively [32,41]. Because interstices are available in α' at similar positions as found in the ferrite [32], the N-solubility in α' is also expected to be lower than in the γ unit cell. The low solubility enables N-rich phases (Fe_2N, Fe_3N) to precipitate in the martensitic microstructure even in the presence of lower concentration of nitrogen in solid solution [18]. Also important is the enhanced nitrogen diffusivity in the martensitic steels as compared to austenite, discussed in Section 3.2.

Because of the chromium depletion above 420 °C [16,18,24,40,42,43], CrN was also indexed in Fig. 2 for 450 °C, which is denoted specially by the peak at ~63°. Chromium presents high affinity with nitrogen and presents enhanced mobility from substitutional sites at such thermodynamic conditions, segregating CrN preferentially at grain boundaries [15,18,32]. As

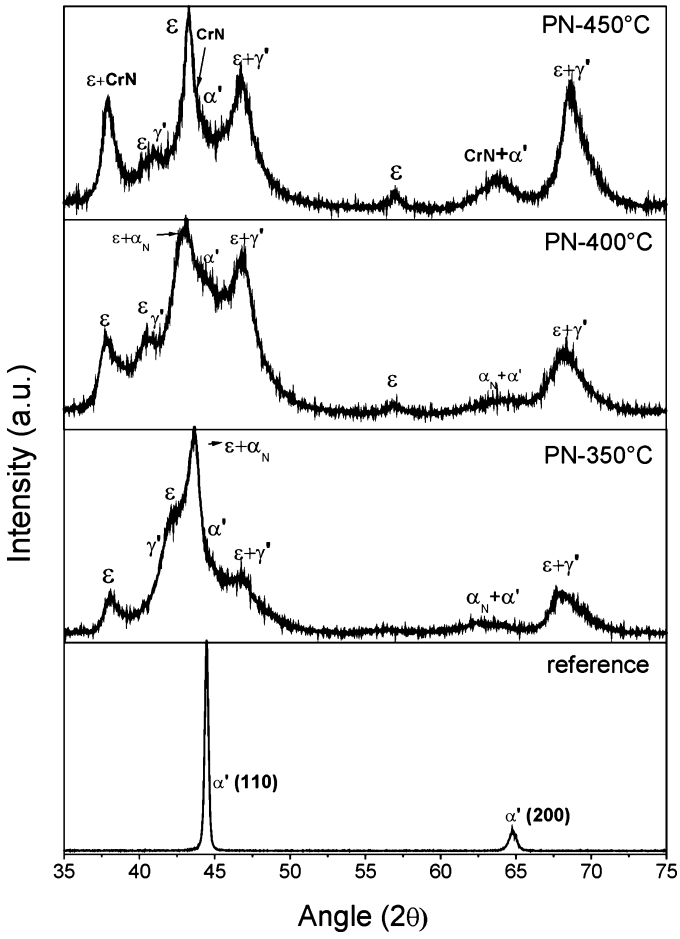

Fig. 2. X-ray diffractograms of SMSS samples plasma nitrided (PN) at the indicated temperatures. The reference sample (austenitized, quenched and tempered in Ar, but not nitrided) presented only martensite (α') peaks. After PN, the nitride compounds $\gamma'(Fe_4N)$, $\varepsilon(Fe_{2+x}N)$ and CrN, as well as the N-expanded martensite phase (α_N), were formed with respect to the processing conditions.

observed in the work by Fernandes et al. [25] on plasma nitriding and nitrocarburizing on SMSS, chromium nitride content increases with the treatment temperature, whereas the iron nitrides content conversely diminishes.

3.2. Morphology

The progressive microstructure changes, as observed after nitriding, were followed by drastic alterations in the surfaces morphologies. Fig. 3 presents cross-section images of the SMSS nitrided at the three working temperatures. Different etching reagents allowed visualizing the modified regions by electron (Fig. 3a) and optical (Fig. 3c) microscopies, with good agreement in the thickness measurements. In Fig. 3a, the near surface regions modified by PN revealed evident changes in morphology, as compared with the substrate (where grain boundaries were evidenced). In Fig. 3b, the nitrogen/iron concentration (in at.%) is presented as a function of depth for the sample nitrided at 400 °C, quantified by EDS point analysis through the line shown in Fig. 3a – 400 °C case. The N/Fe concentration ratio was constant at ≈0.25 (corresponding to ~25% N) up to approximately 25 μm below the surface. This region is ascribed to the nitride layer, containing ε-$Fe_{2-3}N$ and γ'-Fe_4N phases indexed in the XRD results (Fig. 2). From 25 to 39 μm, still inside the modified layer, the concentration ratio decreased continuously up to zero. Such region can be related to the nitrogen diffusion zone (the expanded phase α_N).

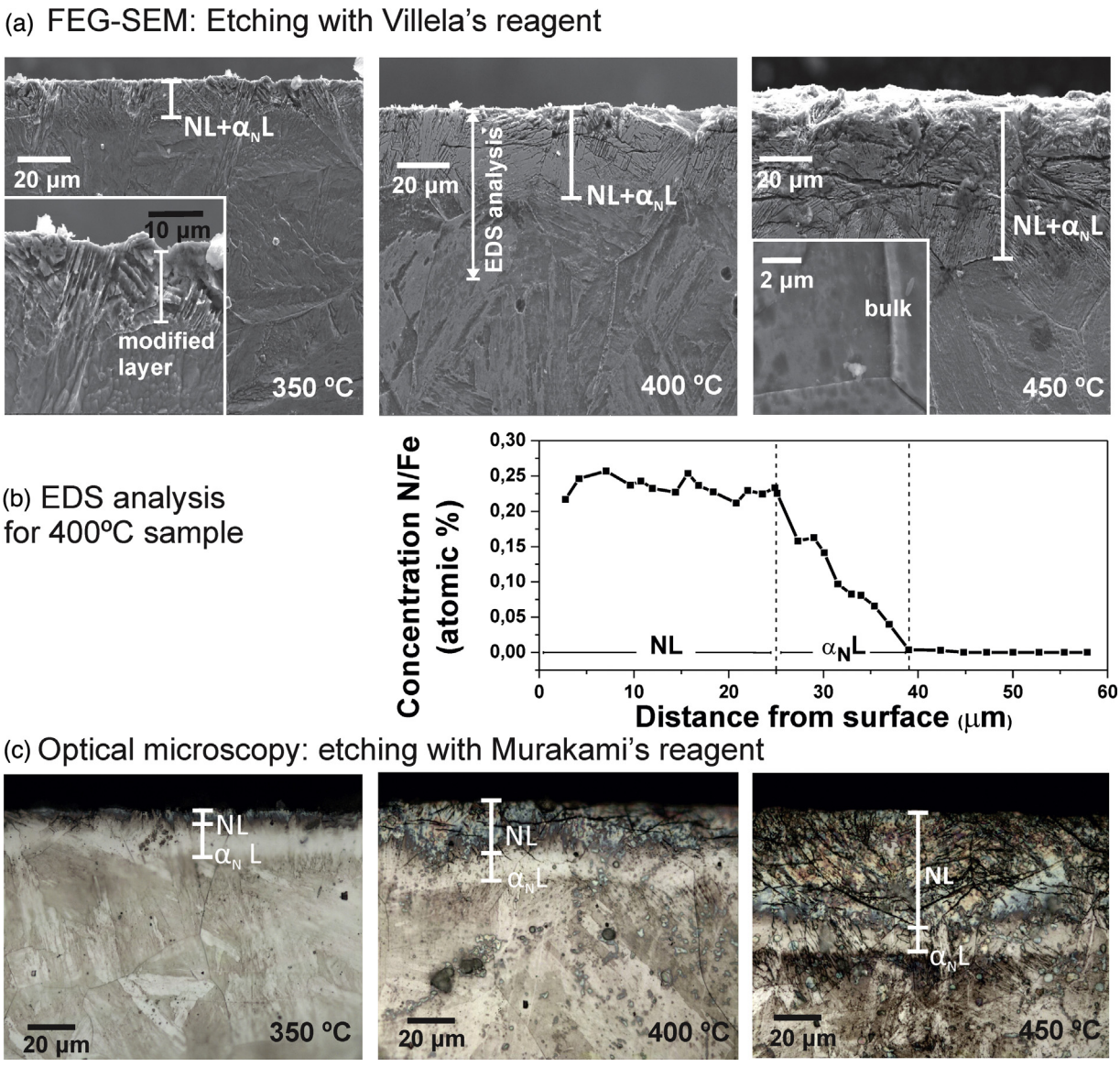

Fig. 3. (a) Cross section FEG-SEM images for the plasma nitrided SMSS samples at the indicated temperatures, etched with Vilela's reagent. Regions indicated by NL and α_NL correspond to nitride (compound) and diffusion layers, respectively. The insets show details of the modified layer at the 350 °C sample, and grain boundaries revealed in the bulk region of the 450 °C sample. (b) The nitrogen/iron concentration, in at.%, obtained by EDS point analysis carried out in several points through the line indicated in (a) for the 400 °C sample. (c) Micrographs obtained by optical microscopy after etching with Murakami's reagent, where NL and α_NL regions can be distinguished. Layers thicknesses for the 400 °C sample are in agreement with regions identified in the N/Fe profile.

Notably, optical microscopy micrographs shown in Fig. 3c enabled to distinguish two different regions in each sample: an upper layer, followed by an intermediate brighter zone contrasting with the substrate beneath. In the 400 °C sample, the layers width (~23 and ~12 μm) agree very well with the different zones identified in the N/Fe profile, Fig. 3c. These regions were ascribed to the nitride (compound) layer and the diffusion layer, respectively labeled as NL and α_NL in all panels of Fig. 3. The higher the nitriding temperature was, the thicker the NL and thinner the α_NL were, which is also in accordance with the XRD results (Fig. 2).

The layer thickness (NL + α_NL) increased with temperature from 16 to 61 μm, as summarized in Table 1. Such thicknesses are larger than the observed in austenitic steels plasma nitrided at the same conditions (from 1 to 10 μm) [16,40,44]. Otherwise, the modified regions were comparable with that produced in other steels with martensitic microstructures as the AISI 420 (from 12 to 50 μm), also treated in similar conditions [19,24,43]. The enhanced nitrogen penetration and the nitriding effects on SMSS are understood based on the particular geometric features of the martensite microstructure, as follows. The nitrogen diffusion in the steel matrix is essentially interstitial, meaning that it is several orders higher than the substitutional-vacancy solute diffusion. By assuming that the

Table 1
Average roughness (*Ra*), layer thickness and hardness of the SMSS HP13Cr plasma nitrided at the indicated temperatures.

Sample	*Ra* (nm)	Layer thickness (μm)	Hardness (GPa)[b]
Reference[a]	15 ± 01	–	4.0 ± 0.1
PN – 350 °C	86 ± 03	16.0 ± 1.7	14.2 ± 0.9
PN – 400 °C	365 ± 23	35.3 ± 3.6	13.5 ± 1.4
PN – 450 °C	437 ± 21	61.2 ± 2.7	11.7 ± 2.4[c]

[a] The SMSS after heat treatment at 1100 °C and oil quenching, with subsequent annealing in Argon.
[b] Average hardness values calculated from hardness profiles of Fig. 7, obtained from instrumented indentation, over the range 300–1100 nm.
[c] See text of Section 3.3.

temperature dependence of diffusivity $D(T)$ obeys the Arrhenius equation:

$$D(T) = D_0 \exp\left(\frac{-Q}{k_B T}\right), \quad (2)$$

where D_0 is the frequency factor, k_B the Boltzmann constant, and Q the activation energy [41], it is reported that $D(T)$ for both interstitial and substitutional solutes is substantially higher in martensite than in austenite [18,32]. This is so because γ (fcc) is a close-packed structure, whereas α′ (body-centered tetragonal) presents a more lower packing density, therefore responding easier to thermal activation, similarly to the mechanism suggested for the ferrite (bcc) microstructure [32]. At 400 °C and in the presence of N-expanded phases, Q_γ is 1.4 eV/atom [18,45], whereas $Q_{\alpha'}$ (in martensitic steel AISI 420) is 0.3 eV/atom [19]. The latter value is about twice as low as that for ferrite [18]. It follows that Q values depend on the N-content in solid solution, for both α′ and γ microstructures. In γ steels, it is suggested [18,45] that the N-expanded phase enhances diffusion (lowering Q) of interstitial atoms, a possible mechanism also valid for α′. On the other hand, when the formation of nitride compounds takes place, Pinedo and Monteiro [43] observed that the activation energy in α′ steels was increased fourfold, so diminishing diffusion rates due to precipitation reactions occurring at the modified layer. The above mentioned references [18,43,45] showed that diffusion in plasma nitrided steels is a complex phenomenon because it is a synergistic process: the dynamic nature of nitride precipitation, the nitrogen solubility in the changing environment, and the mobility of solute atoms, especially chromium, to produce other equilibrium nitride phases. Nevertheless, the martensite microstructure in SMSS enables enhanced nitrogen diffusion conjoined with the low N-solubility, as previously discussed in Section 3.1.

Fig. 4 shows representative FEG-SEM and AFM micrographs of the untreated and nitrided SMSS; Table 1 presents average roughness (Ra) values. The initially mirror-like polished surface (untreated sample) was smooth, presenting Ra = 15 nm, with no significant morphology differences among grains or evidenced grain boundaries. After nitriding, the surfaces were texturized, featured by polyhedral slabs with irregular height distributions with respect to the top view, increasing the measured mean roughness in one order of magnitude. Such structures have similarities with grain boundaries disclosed by etching, as shown in the inset of Fig. 3a (450 °C sample). Thus, they are ascribed to grains with different crystallographic orientations, as well as microstructures within individual grains (e.g., twin boundaries), which response to the plasma processing depended on their specific orientations.

The plasma treatment affects morphology by means of at least two phenomena. The first and obvious one is the anisotropic *swelling* of individual grains. An orientation-dependent nitrogen diffusion and storage rates in SMSS can be assumed, similarly as observed for austenite steels. Williamson and co-workers [45] reported that in fcc austenitic steels submitted to ion implantation, nitrogen diffuses faster in the [1 0 0] direction than in the [1 1 1] direction, whereas solubilization was higher in the (2 0 0) planes than in the (1 1 1) planes parallel to the surface. This analysis was taken into consideration the elastic constants of crystallographic directions, and the relative XRD peak intensities of γ and γ_N (N-solid solution in the γ matrix). Because of the overlapping of α′, α_N and nitride peaks as shown in Fig. 2, such phases are not well resolved in the present case and a similar comparison is not possible. However, elastic anisotropy among crystalline directions is well established for martensitic steels – for instance, elastic modulus is about 75% larger in the (1 1 0) plane than in the (2 0 0) plane [46,47]. Thus, lattice expansions (the increase in the crystallographic parameters and corresponding peak shift from α′ to α_N) would be expected to be larger in the latter plane.

Swelling due to nitrogen incorporation and nitrides precipitation is also important in generating stresses. Austenitic and martensitic phases have marked differences in the nitrogen solubility and diffusivity between them. Nitrogen atoms in solid solution prevail in the former, whereas nitride precipitates prevail in the latter [18]. Both effects generate internal elastic stresses by locally distorting the crystalline structures. Stinville and co-workers [48] studied in details the swelling phenomenon produced by PN in austenitic AISI 316 steel grains. They observed a strong dependence of swelling with the grain orientation. Such effect was maximum for grains with the [0 0 1] direction normal to the surface, and minimum for the [1 1 1] direction, which is in accordance with the aforementioned results from Williamson et al. [45] for N-diffusion in the austenitic matrix. Experimental elongations as high as 20%, lateral stresses of approximately −2.5 GPa, and analytical considerations carried out by the authors [48] were consistent with two additional phenomena contributing with the nitrogen lattice expansion: residual stresses caused by neighboring grains (which constrain dilation), and, in a major extent, plastic strain caused by the γ_N phase. In martensitic microstructures, those effects may act

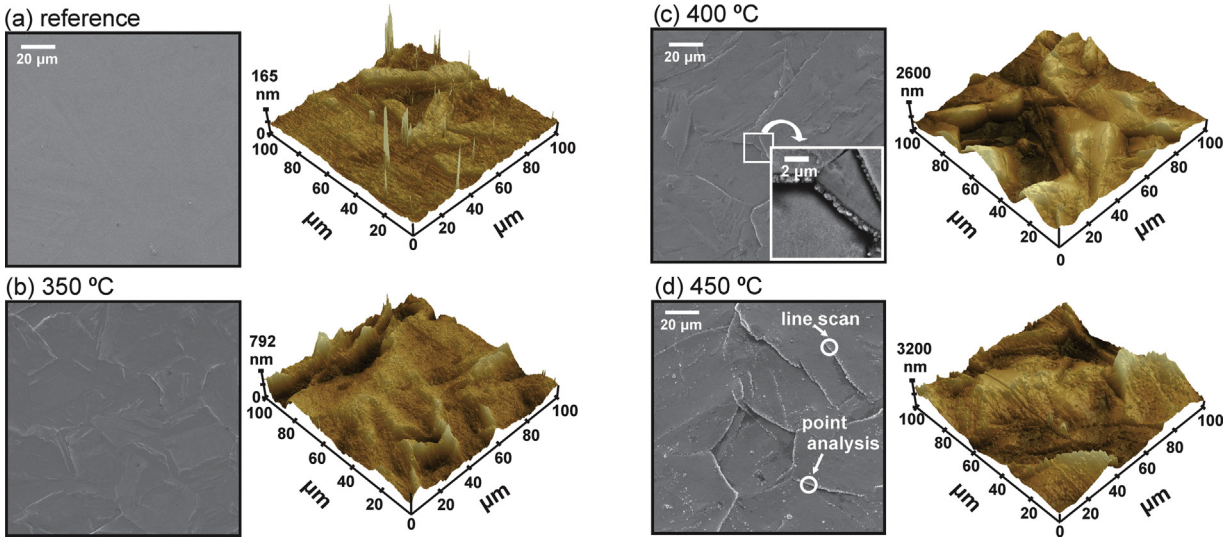

Fig. 4. FE-SEM and AFM micrographs of (a) reference and (b, c, d) plasma nitrided SMSS surfaces, at the indicated temperatures. The inset in (c) corresponds to the magnified region indicated by the square. Regions indicated in (d) were EDS analyzed in Fig. 5.

in different proportions, given the relatively high N-diffusivity and low solubility rates, what demands further investigations. Analysis of Fig. 4 suggests that swelling in SMSS is in the range of hundreds of nanometers, similarly as measured by [48] in AISI 316.

A second possible explanation to the surface morphology observed in Fig. 4 is the *ion sputtering*, removing individual atoms from surfaces by momentum transference. Manova et al. [49] observed that the sputtering rate in steels is orientation dependent, eroding different grains at different rates, also producing steps and kinks at twin boundaries inside individual grains. Notwithstanding, the ion energies in that study were much higher (10^4 eV) than that applied in the present samples (<10^3 eV), which allowed increased sputtering rates. In addition (as it can be observed in the inset of Fig. 4c, 400 °C case), in SMSS the abrupt changes in topography were larger in grain boundaries than in the steps inside individual grains, differently than that reported in [49]. Therefore, sputtering by plasma species has minor effect in producing such an intense changes in the SMSS morphologies, and is likely associated with the "short-range" roughness on the top of slabs, observed in Fig. 4.

Several spherical microstructures were also observed on the surfaces nitrided at 400 and 450 °C, essentially along grain boundaries (see the inset of Fig. 4, 400 °C case). The formation of spherical-shaped precipitates in stainless steels submitted to thermal and nitriding processes have been ascribed to chromium nitrides [50] and $M_{23}C_6$ carbides [38,51,52]. Kong et al. [50] investigated the gas nitriding and tempering effects on the Cr–Ni–V martensitic steel. They observed round chromium nitrides formed at the outermost surface and chromium carbides in inner regions, where diffusing N atoms eventually could substitute C atoms. Those studies were conducted at 600 °C or higher. In γ stainless steels, carbides are formed in the range 550–800 °C [32]. As previously mentioned, the CrN compound can be formed preferentially at grain boundaries above 420 °C [15,18].

Differently from the previous cited works, in the present case, elemental analyses by FEG-SEM and EDS, both at 400 °C and 450 °C samples, were consistent with a $M_x(C,N)_y$ compound, where M is mainly Fe. Because lateral resolution in EDS is much greater (in the order of μm) than the probe size (nm) [53], analyses in Fig. 5 were carried out in spherical microstructures aggregated in a region with approximately 1 μm width, situated at grain boundaries on the 450 °C sample, as indicated in Fig. 4d. EDS spectra from point analysis, shown in Fig. 5a, disclosed that carbon and nitrogen concentration increased more than twofold at the spheroid structures, whereas chromium decreased to less than a half as compared to the remained surface. Fe slightly increased inside the microstructures, and other alloying elements (Ni, Mo) slightly decreased. No significant changes were observed in O contents among the different analyzed regions. Additional EDS line scan (Fig. 5b) corroborates with the above results, where Cr concentration clearly decreases and C and N clearly increased at the agglomerate region. Ni and Mo (not shown) slightly decrease and Fe increases. Thus, it is possible to assert that the spheroid structures lying at grain boundaries are better ascribed to iron carbides or nitrides, although other alloying elements such Ni and Mo cannot be discarded.

Perhaps, such spheroidal structures comprise residual iron carbides from the quenching heat treatment (Section 3.1), not detected by XRD, which were partially substituted by nitrides in a mechanism similar to the aforementioned Kong's [50] proposal for Cr(C,N) phases. One could assert that C-content in SMSS is too low – carbides were not reported in plasma nitrided austenitic steels [15–17,26,27], which contain about 10 times more carbon than SMSS. However, the carbon mobility in the martensite microstructure is significantly higher than in the austenite, since activation energies Q in Eq. (1) are 0.29–0.88 eV [20] and 0.58–1.29 eV [18], respectively.

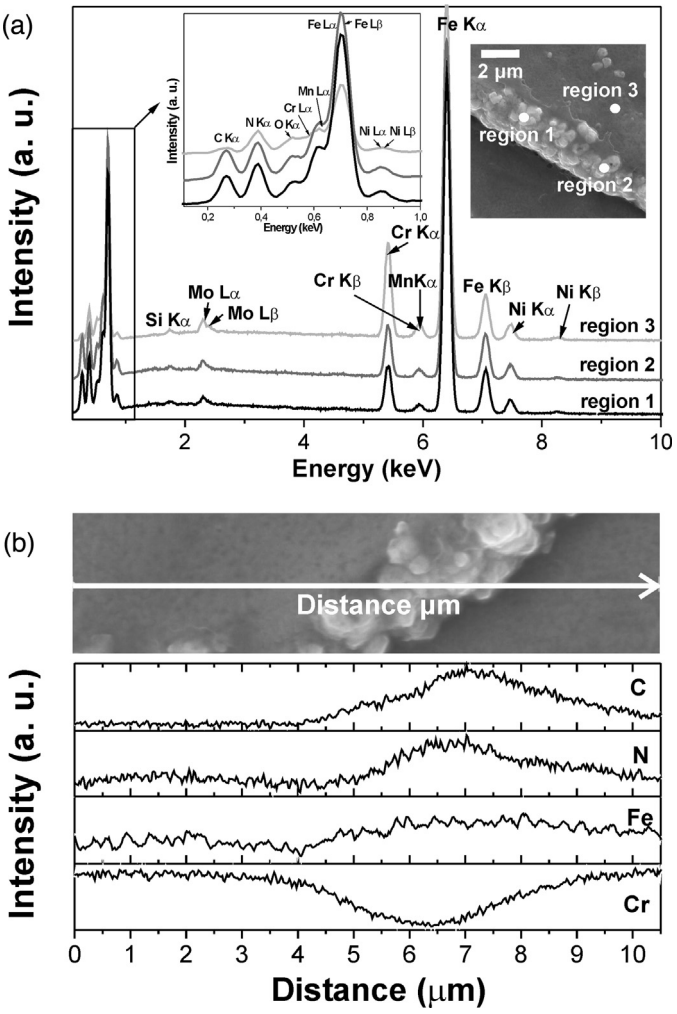

Fig. 5. FEG-SEM image and EDS analysis of the sample plasma nitrided at 450 °C, corresponding to regions indicated in Fig. 4d: (a) point analysis and (b) line scan. Abrupt differences in topography are ascribed to grain swelling (see text for details). In (a), points indicated by numbers correspond to the elemental analysis performed in the surface and in the spherical bright structures lying at grain edges.

3.3. Hardness and elastic modulus

Images of typical indentation imprints, produced at the final 400 mN applied load, are presented in Fig. 6 for the reference sample and the one nitrided at 450 °C. On the untreated surface, the indentation residual depth was about 2 μm; the surface around indentations presents slip bands and some pile-up process (inner material plastically displaced to the imprint edges). The imprint inspection after plasma nitriding clearly showed evidences of surface hardening. A half reduced residual depth was observed, whereas the surface sink-in took place at the indentation edges. Sink-in correlates with the material's ability to undergo strain-hardening, whereas pile-up denotes the poor degree of such property. Generally, the ratio between elastic modulus and yield strength is low for sink-in (as it is the case of strain-hardening metals or non-strain hardening materials such as ceramics) and large for pile-up (as observed in some metals) [54]. The imprint corners, notably in the 450 °C sample, also presented radial cracks, denoting some brittleness of the top surface layer under loading. Such crack occurrence can be attributed to the formation of nitride compounds ε, γ′ and CrN, predominating over α_N.

Fig. 7a presents hardness profiles of the reference and plasma nitrided surfaces. Differences among instrumented indentation

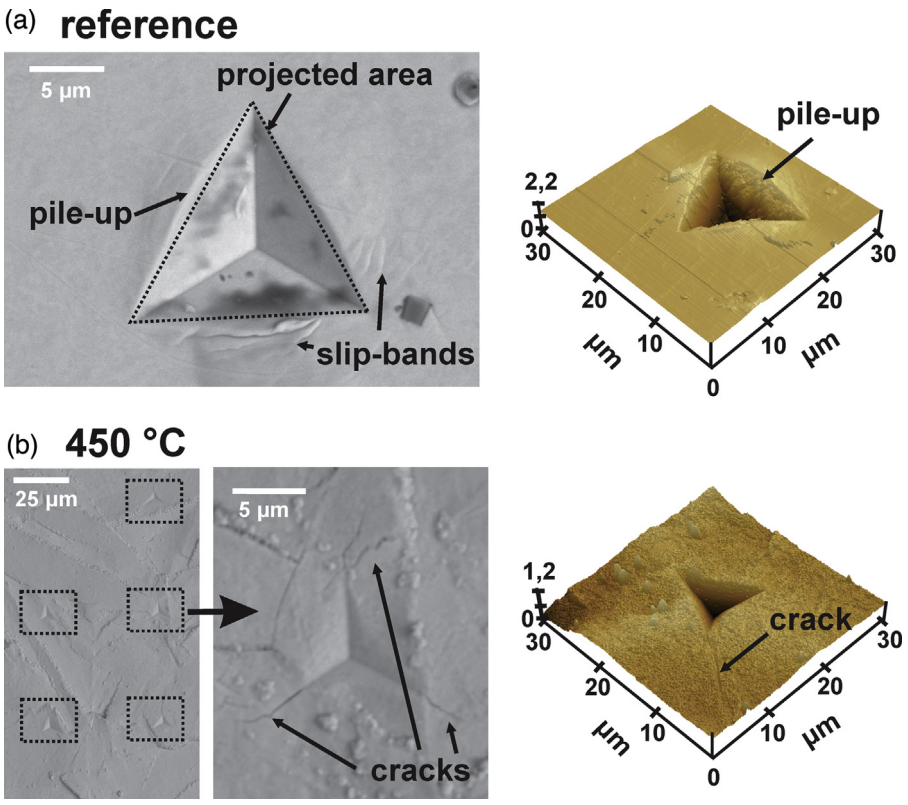

Fig. 6. FEG-SEM and AFM micrographs of indentation imprints produced with 400 mN applied load on (a) reference sample and (b) the one plasma nitrided at 450 °C. Slip bands and pile-up (deviations from the projected area) were observed on polished SMSS before nitriding. The lower magnification in (b) aims to illustrate the roughness and grain anisotropies effects in different tested regions. An imprint highlighted by a square is magnified, disclosing cracks at the imprint corners.

(dark symbols) and microhardness (bright symbols) profiles are due to the specific measuring methodologies, as stated in Section 2. The near surface hardening observed in the untreated sample (a decreasing profile from 5.5 GPa to ~3.5 GPa at 400 nm) is due to residual stresses induced by mechanical polishing. After nitriding, the average hardness values obtained by instrumented indentation presented initially slight increases with depth and large error bars, notably in the 450 °C sample. In spite of the contact stiffness correction [37] to minimize roughness effects on the results, the previously discussed grain anisotropies and sputtering rates (Section 3.2) were significant for this temperature. Such dispersion is also ascribed to errors caused by asymmetric imprint areas, as it can be seen in Fig. 6b, affecting hardness calculation by the usual analytical method [36]. Indeed, the extension of the 450 °C profile by microhardness tests (which are less affected by roughness) presents higher mean values and lower dispersions. Nevertheless, all the hardness profiles reached a plateau at around 300 nm depth, an expected behavior by considering the estimated layer thicknesses, Table 1. According to Saha and Nix [30], the plastic deformation field produced by indentation is constrained inside the hard coating, provided that the maximum depth is less than 10% the coating thickness. Thus, the substrate beneath do not affect hardness values computed under such circumstances. At deep penetration depths, reached by microhardness tests in Fig. 7a, profiles decreased continuously toward the substrate value. Notwithstanding, the 350 °C profile seems to present a shift in inclination at around 4000 nm depth. To investigate further such an effect, instrumented indentation was also carried out directly on the cross sections. Fig. 7b shows hardness values for the 350 °C sample. Hardness of the nitride layer NL (which is about 5 μm in thickness, see Fig. 3b) was ~12 GPa, in accordance with Fig. 7a. On the other hand, the diffusion layer (the region with nitrogen in solid solution, lying from ~5 to ~16 μm) presented smaller hardness values.

For comparison purposes, Table 1 summarizes the calculated average values for the modified surfaces, over the range 300–1100 nm. Hardness mean values of the SMSS plasma nitrided at 350 and 400 °C were 12–15 GPa, which are comparable to values reported for austenitic (AISI 304 and 316) [16,55] and martensitic (AISI 410 and 420) [19,56] steels treated at the same temperature range. In austenitic steels, the expanded γ_N phase predominated, whereas in martensitic ones α_N and nitride compounds were identified, similarly as in the present situation. By increasing the treatment temperature to 450 °C, the amount of nitride compounds increased as well, and the α_N contribution diminished (Fig. 2). In spite of that, hardness profile from instrumented indentation tests for 450 °C was lower than that for other conditions (11.7 GPa), which can readily be attributed to the large dispersion caused by roughness (Table 1) and brittleness around imprints (cracks in Fig. 6b). In this case, average of microhardness values obtained at 10% the layer thickness was 12.6 GPa, which is statistically similar to the other temperature values. Moreover, scratch tests also demonstrated such surface strengthening, as discussed further.

In spite of conspicuous differences observed in crystalline structure, morphology and hardness, the elastic modulus profiles of plasma nitrided SMSS (Fig. 8) were statistically similar among the treated surfaces, and from those with the reference SMSS (~240 GPa). Such behavior was also reported for austenitic [16] and martensitic [24] steels. The large error bars (notably in 450 °C) are attributed to roughness and grain anisotropies, as previously discussed. However, an additional explanation can explain both dispersion and the observed statistical invariability in elastic modulus, which connects directly to the physical basis of that property. Elastic deformations in the indentation perimeter depend strictly on the net bond forces connecting atoms in the crystal lattice, and they can reach wider regions inside the bulk than the plastic deformation field [54]. If the produced compounds are tiny nitride

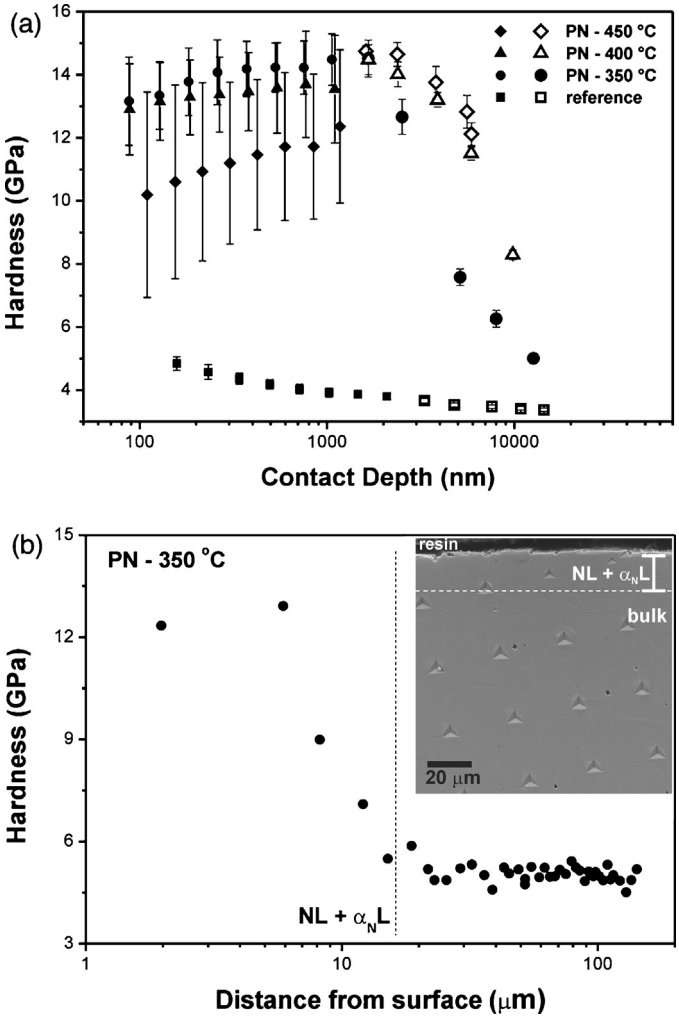

Fig. 7. (a) The hardness profiles of reference and plasma nitrided SMSS. Dark symbols correspond to instrumented indentation results, whereas bright symbols indicate microhardness test values. (b) Instrumented indentation carried out in the cross section area of the SMSS plasma nitrided at 350 °C, with the corresponding hardness values with respect to the distance from surface. The dashed line indicates the mean thickness of nitride (compound) and diffusion layers (NL + α_NL).

precipitates embedded inside martensite grains, or nitrogen atoms occupying interstices, the residual stresses caused in their vicinity produce an average elastic response that is only a deviation from that observed for the stress-relieved matrix. On the other hand, changes induced by ion nitriding (lattice distortion and nitride precipitates) do affect twinning and dislocation gliding mechanisms, which are responsible for the material's plastic deformation.

Based on these assumptions, and because nitride compounds were identified in all working temperatures (Fig. 2), it is possible to assert that the precipitate-dispersion hardening [34] is an important effect at near surface of nitrided SMSS. In such a mechanism, hard and small precipitates (ε and γ') act as obstacles to dislocation movement, increasing the material's strength. Another possible mechanism is the Cottrell atmosphere, in which interstitial N atoms (the α_N phase) increase plastic strength by migrating to vacant sites around the dislocations and pinning them.

3.4. Nanoscratch

Fig. 9 presents typical scratch penetration profiles for the reference sample and the sample plasma nitrided at 350 °C. These scratch tests were carried out with ramping load up to 400 mN. Samples nitrided in the remainder conditions (400 and 450 °C) presented similar profiles, that is, scratch grooves constrained to the modified layers and shallower than the reference sample. In addition, the maximum penetration depths were similar to those observed in nanoindentation imprints, Fig. 6, using the same maximum load. In Fig. 9, after nitriding at 350 °C, the maximum penetration depth was reduced 36% (from ~2 to 1.3 μm), whereas the elastic recovery after unloading increased from 18% to 55%, which is in agreement with the presence of a strengthened case containing expanded phase and nitrides.

These results indicated a superior strengthening under scratch of SMSS by plasma nitriding as compared to AISI 304 and 316 steels [55]. Because of the severe irregularity in morphology, as shown in Fig. 4, the same profile analysis was not possible for the 400 and 450 °C samples. To investigate further the nitriding effects on the scratch resistance, grooves were qualitatively analyzed by FEG-SEM, as follows.

The grooves morphologies produced on nitrided SMSS, shown in Fig. 10, are completely different from that on the reference surface. As scratches on the reference sample were nearly straight, the sliding tip experienced lateral track deviations in the nitrided

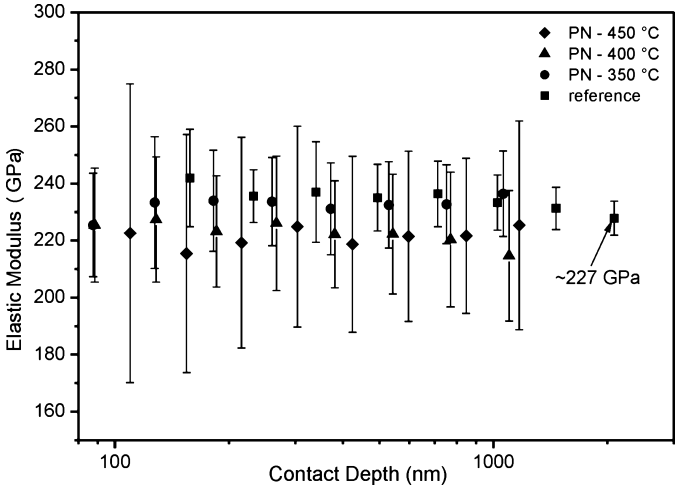

Fig. 8. The elastic modulus profiles of reference and plasma nitrided SMSS. Both the large error bars and statistical invariability of elastic modulus can be understood through the physical basis of the material's elastic response – see text for details.

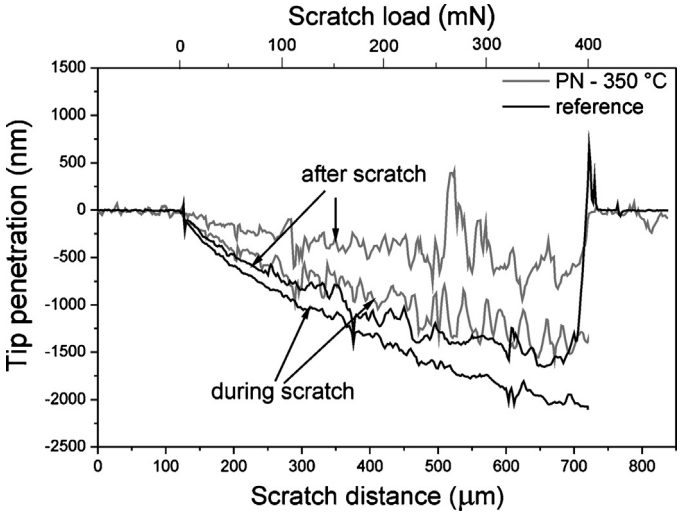

Fig. 9. Penetration profiles recorded during scratch tests with constant loading up to 400 mN, and the residual profile of grooves, for the reference SMSS and the surface plasma nitrided at 350 °C.

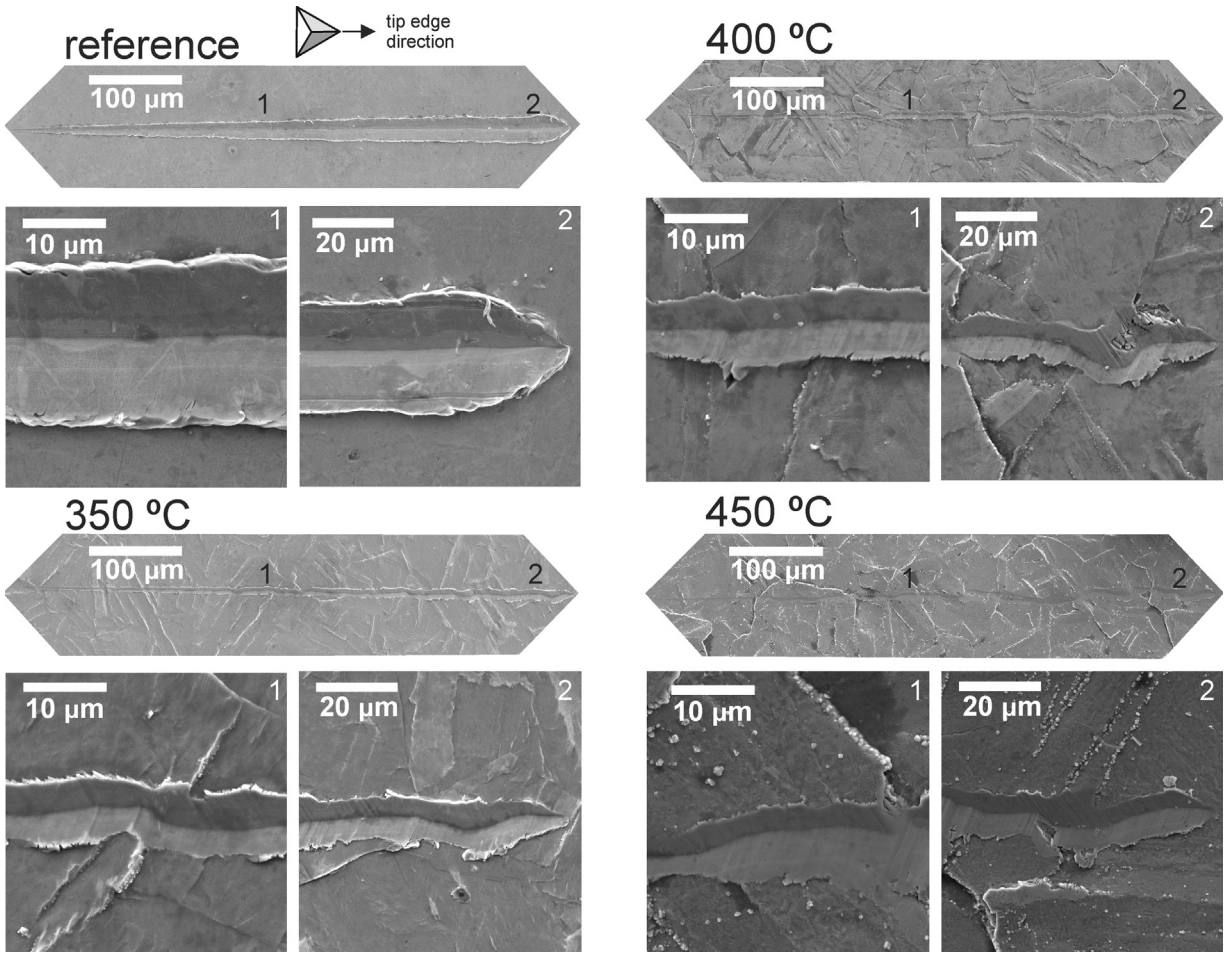

Fig. 10. FEG-SEM images of typical scratch grooves produced on the reference and plasma nitrided SMSS at different working temperatures. Numbers in the entire tests images indicate regions magnified below them. The applied load increased linearly up to 400 mN, for 600 µm length.

surfaces. Moreover, this anisotropy seems to be working temperature dependent. Similar behavior was also observed in plasma nitrocarburized austenitic steels [40]. Such result corroborates with orientation-dependent anisotropies in the N-diffusion and N-precipitates formation, as discussed in Section 3.2. The groove widths were narrower on the hardened nitrided surfaces (reducing from 20 to ~8 µm at the scratch middle region). As the reference sample's groove was smooth, the grooves in nitrided samples were rough through the entire scratch lengths, suggesting the occurrence of a stick-slip mechanism, in which the tip interaction with hard precipitates hinders its movement. The deformation energy accumulates at the tip edge, so being suddenly released.

Differently from the observed under normal loading (indentation in Fig. 6), and in spite of the different loading rates, neither cracks nor chipping were noticed in scratch tests after nitriding – only exception was the crushed grain boundary region, near the groove's end in the 400 °C sample. Actually, scratches on nitrided samples disclosed ductile-like features, notably the occurrence of pile-up (material plastically removed to the track edges), which intensity seems to decrease from the reference to the 450 °C-treated surface. These discrepancies are understood on the basis of the different stress distribution in normal (indentation) and tangential (scratch) loading [54]. The plastic deformation field in indentation tests reaches deep regions, which, in plasma nitrided surfaces, constitute a graded texture of hard precipitates, interstitial nitrogen and residual stresses. On the other hand, the stress distribution in scratch tests also comprises tangential forces due to the moving tip, so that plastic deformation is constrained around the tip and at shallow depths.

4. Conclusions

Supermartensitic stainless steel HP13Cr was plasma nitrided at temperatures 350, 400 and 450 °C. The starting condition was a fully martensitic microstructure, achieved by heat treatment at 1100 °C and oil quenching. The nitriding process substantially changed the surface morphology, microstructure, and tribo-mechanical response as compared to the reference surface, as follows.

- Because of the synergistic effect of high diffusivity and low solubility of nitrogen in the martensitic structure, nitride phases ε-$Fe_{2+x}N$ ($0 \leq x \leq 1$) and γ'-Fe_4N were formed in all working temperatures, in addition to nitrogen in solid solution (α_N). Layers comprising nitrides and diffusion zones presented thickness ranging from 16 to 61 µm, according to the treatment temperature. At the outermost surface, the crystalline orientation-dependent diffusion (the swelling phenomenon) and sputtering rates produced an irregular topography with averaged roughness about 400 nm for the highest working temperature.
- The surface hardness, measured by instrumented indentation, increased from 3.8 to ~14 GPa in all the working temperatures. The elastic modulus presented no statistically significant differences as compared with the reference surface, with a value

around 230 GPa. Such behavior is understood based on the different extent of plastic and elastic deformation fields (ruling hardness and elastic modulus measurements, respectively) inside the precipitate-containing texturized layers.

- Strengthening of the nitrided surfaces was also observed in scratch tests. Under tangential loading, a hardened-ductile like character was disclosed (groove widths reduced from 20 to ~8 μm), with no evidences of cracking, chipping or brittle fracture. In spite of singularities concerning the different loading regimes, as in indentation tests, the precipitation hardening plays an important role in the SMSS scratch resistance.
- The results corroborate with the effectiveness of plasma nitriding in the surface modification of supermartensitic stainless steels, supporting further studies in aspects of interest for this alloy.